PCCP

ROYAL SOCIETY OF CHEMISTRY

PAPER

View Article Online
View Journal | View Issue

Cite this: *Phys. Chem. Chem. Phys.*, 2026, **28**, 6044

Received 7th November 2025,
Accepted 11th February 2026

DOI: 10.1039/d5cp04304b

rsc.li/pccp

Controlling the charge of single nanoparticles in an ion trap

Sophia C. Leippe, Kleopatra Papagrigoriou, Carl Behrendt and Björn Bastian *

Control over the charge of a nanoparticle (NP) in a radiofrequency ion trap is crucial for mass spectrometric and charge dependent investigations of single NPs. We show how this is achieved for positively charged silica NPs (nominal diameter 100 nm, 350–1400 *e*) with a simple experimental realization using a standard cold cathode gauge. The change of the NP charge is the result of processes, where electrons and cations interact with the trapped NP. We investigated how NP charging depends on pressure and gas type as well as on the ion trap amplitude and waveform, which can be used for charging and discharging in a wide NP charge range. The measurement of average charging rates as a function of the NPs' charge for widely varied experimental parameters allows us to capture essential relationships between gas pressure, NP charge, trap potential and net charging rates. The acceleration of gas cations by the trap potential is shown to be the driver of electron abstraction from the NP by gas cations and thereby makes high NP charges accessible.

Open Access Article. Published on 18 February 2026. Downloaded on 5/10/2026 3:55:05 AM.
This article is licensed under a Creative Commons Attribution 3.0 Unported Licence.

Introduction

Obtaining information on the intrinsic properties of single nanoparticles (NPs) remains a major challenge in nanoscience. While ensemble experiments suffer from chemical and physical heterogeneity, most single particle techniques involve the characterization of supported NPs. In contrast, using a Paul-type ion trap allows to non-destructively determine the absolute mass and charge of individual NPs isolated in the gas phase. This approach was first realized and refined by the groups of Gerlich and Anderson.[1,2] The cryogenic Single Nanoparticle Mass Spectrometry (NPMS) instrument we use contains a Paul-type trap and is specifically designed for surface adsorption experiments as well as absorption and fluorescence spectroscopy of single NPs.[3–6] To achieve long-term stability of a cationic NP in the ion trap (typically operated at 25 kHz frequency and 200 V amplitude for 100–1000 MDa NPs)[3] and high signal quality, it was found beneficial to charge the NPs up to charges of around +1000 *e*. The present investigation of the charging behavior of single NPs sheds light on the charging mechanisms and allows to change the NP charge in a controlled manner in both directions which simplifies experiments and is crucial to investigate the influence of the NP charge on other NP properties.

The charge of individual NPs in the gas phase can be manipulated by exposing them to an electron gun,[1,7] ion beam,[7] soft X-rays,[8] UV light,[9,10] high electric fields[11] or a cold cathode gauge.[2,3] Different charging techniques evoke different charging mechanisms. Direct photoelectric charging happens when a NP absorbs photons and subsequently electrons are emitted. Diffusion charging occurs when charge carriers such as gas ions collide with a NP due to their Brownian motion followed by charge transfer.[8,11] Excited rare gas species might drive Penning ionization on a NP surface.[12] The underlying mechanisms of photoelectric charging of individual SiO_2 NPs in an ion trap by exposing them to soft X-rays have been studied previously.[8] Furthermore, electron bombardment has been used to charge gold clusters as well as 500 nm SiO_2 NPs in an ion trap.[13,14] Diffusion charging of aerosol particles by gas ions has been theoretically described[15] and experimentally investigated using high electric fields or soft X-rays.[11] In this study, we investigate charging of individual NPs in an ion trap by interactions with ions and electrons.

While direct photoelectric charging takes place throughout the NP volume, diffusion charging only happens at its surface. Charge carriers can interact with the NP surface in different ways. Electrons can attach to the NP, provided their kinetic energy is low enough to be sufficiently dissipated upon the first collision,[16] discharging a cationic NP. Sufficiently fast electrons can perform electron impact ionization of the NP,[14] and thus further charge a cationic NP. Moreover, electrons can collide with gas atoms or molecules and thereby generate gas cations and secondary electrons by electron impact ionization. In principle, fast electrons with a kinetic energy above the ionization potential (IP) of the gas are required to produce gas cations, while slow electrons more likely attach to the NP.

Wilhelm Ostwald Institute for Physical and Theoretical Chemistry, Leipzig University, Linnéstraße 2, 04103 Leipzig, Germany. E-mail: bjoern.bastian@uni-leipzig.de

This journal is © the Owner Societies 2026

Open Access Article. Published on 18 February 2026. Downloaded on 5/10/2026 3:55:05 AM.
This article is licensed under a Creative Commons Attribution 3.0 Unported Licence.

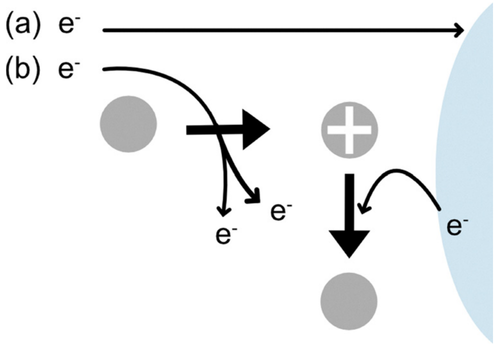

Fig. 1 Scheme of (a) electron attachment to the NP (light blue), and (b) electron abstraction from the NP by gas (gray) cations. For (b) an electron coming from the cold cathode gauge collides with a gas atom, forming a gas cation (white plus sign) and secondary electrons by electron impact ionization. The gas cation then abstracts an electron from the NP surface and becomes neutral.

Gas cations can abstract electrons from the NP, further charging a cationic NP. Fig. 1 illustrates the mechanisms of electron attachment to the NP and electron abstraction from the NP by gas cations, which we expect to be the two dominant mechanisms that influence the NP charge in case of moderate electron kinetic energies.

In this study, a cold cathode gauge which is directed toward the ion trap is used to charge or discharge NPs trapped in the NPMS instrument. This is an inexpensive and practical method because cold cathode gauges are readily available in many vacuum setups. Cold cathode gauges have been used previously to charge individual NPs in a gas-filled ion trap but the underlying mechanisms have not been investigated. The cold cathode gauge works based on electron impact ionization and produces gas cations, electrons, and photons. Based on the mean free path, the number of gas cations emitted by the gauge that could reach the trap center is negligible above a pressure of 2×10^{-3} mbar (see Fig. S1a in the SI). Electrons that would escape the gauge region despite the permanent magnetic field could reach the trap center in the entire pressure range investigated here. Ultraviolet radiation from the gas discharge and X-ray bremsstrahlung from electrons striking the anode can produce electrons on remote surfaces by the photoelectric effect. Electrons can furthermore collide with gas atoms or molecules and thereby ionize or excite them and generate secondary electrons.[2]

We investigated positively charged NPs and therefore define charging as increasing their positive charge and discharging as decreasing their positive charge. The total charging rate is expressed as the difference $k_{\text{total}} = k_{\text{abst}} - k_{\text{att}}$ of the electron abstraction and attachment rates. Charging over a time period Δt leads to a net change of the NP charge $\Delta Q = k_{\text{total}}\,\Delta t$ that can be measured by mass spectrometry.[1] k_{total} is influenced by the experimental conditions that determine which charging mechanism dominates. One of the influential parameters is expected to be the buffer gas type that is leaked into the trap: with a higher electron impact ionization cross section σ_{EI} of the gas, more gas cations are produced (see Fig. 2(1)) that can abstract electrons from the NP, increasing the electron abstraction rate k_{abst}. Similarly, at a higher pressure, more gas cations are produced (see Fig. 2(2)), also increasing k_{abst} and thus k_{total}. If the origin of electrons and the trap center were in close proximity to each other, one would expect a linearly increasing number of primary electrons with the pressure and a quadratically increasing number of cations produced by them so the pressure dependence of k_{total} would be quadratic (see Fig. 2(3a)). When considering a distance between the origin of electrons (*e.g.* photoemission from the metal surface of the tube connecting the gauge to the trap chamber) and the trap in the present setup, this scenario only holds for low pressure without collisions. The situation is more complex for increasing pressure: collisions with gas atoms reduce the electron mean free path, counteracting the increase of primary electrons, while also secondary electrons are produced by electron impact

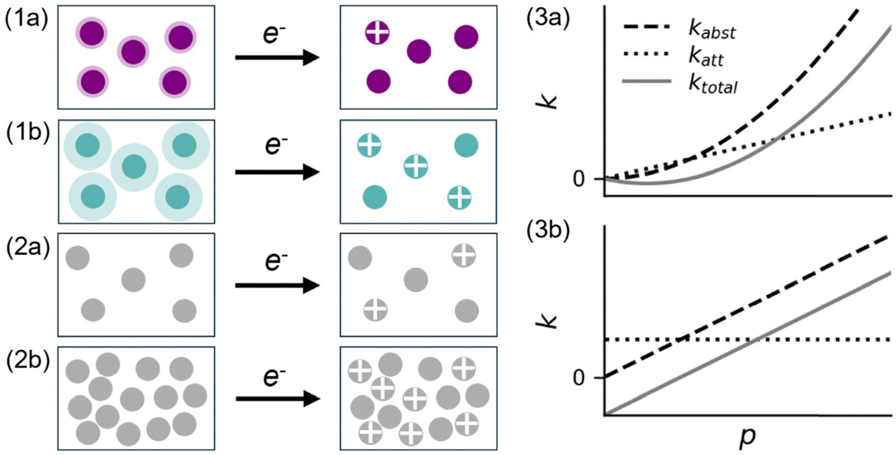

Fig. 2 Schematic of how more gas cations are generated (1) when using a gas with a higher electron impact ionization cross section σ_{EI} (1a to 1b), represented by the area of a transparent circle or (2) when increasing the pressure (from 2a to 2b). (3) Pressure dependence of the charging rate k_{total}. The electron abstraction rate k_{abst} and the electron attachment rate k_{att} depend on the number of gas cations and electrons, respectively. With $k_{\text{total}} = k_{\text{abst}} - k_{\text{att}}$, the pressure dependence of k_{total} is quadratic for a linearly increasing electron number (3a) and linear for a constant electron number (3b).

Open Access Article. Published on 18 February 2026. Downloaded on 5/10/2026 3:55:05 AM.
This article is licensed under a Creative Commons Attribution 3.0 Unported Licence.

ionization and add up to the number of electrons in the trap center. In the case of a constant number of electrons, k_{att} is constant and therefore the pressure dependence of k_{abst} and k_{total} is linear (see Fig. 2(3b)), which will turn out to be a good approximation for the empirical data below.

Apart from the gas type and pressure, k_{total} should depend on the NP charge. The IP of the NP rises with its charge and therefore gas cations experience a higher Coulomb repulsion. Conversely, electrons approaching the NP experience a higher Coulomb attraction by highly charged NPs. Therefore, we expect that a high NP charge fosters electron attachment while a low NP charge fosters electron abstraction by gas cations. These considerations can be quantified with the collision cross sections of cations and electrons with a positively charged NP derived in Section S10 of the SI,

$$\sigma_{\text{coll}}^{\text{cation-NP}} = \pi R^2\left(1 - \frac{Qe}{4\pi\epsilon_0 R}\frac{1}{E_{\text{kin}}}\right), \qquad (1)$$

$$\sigma_{\text{coll}}^{\text{electron-NP}} = \pi R^2\left(1 + \frac{Qe}{4\pi\epsilon_0 R}\frac{1}{E_{\text{kin}}}\right), \qquad (2)$$

with the NP charge Q and radius R, elementary charge e, vacuum permittivity ϵ_0, and initial kinetic energy E_{kin} of the cation or electron, respectively. The collision cross section with cations decreases with increasing Q and vanishes when the initial kinetic energy is smaller than the Coulomb potential at the NP surface. In contrast, the collision cross section with electrons grows with increasing Q.

Considering the energy balance for electron abstraction by gas cations is instructive to estimate the maximum NP charge for which electron abstraction would be energetically possible in the absence of the ion trap. If the gas IP exceeds that of the NP, electron abstraction is favorable with the energy gain

$$\Delta E_{\text{abst}} = \text{IP}_{\text{gas}} - \frac{Qe}{4\pi\epsilon_0 R} - W, \qquad (3)$$

where Q is the NP charge, R the NP radius, ϵ_0 the vacuum permittivity and W the work function (see Section S11 for details). The second term approximates the NP surface potential by the Coulomb potential. While previous studies have shown that it tends to underestimate the actual surface potential, it remains a useful approximation for the purpose of this analysis.[8,13] For NPs, the work function can differ from that of the bulk due to size and surface structure effects.[17] Furthermore, adsorbed gas and impurities from the atmosphere on the NP surface may alter the work function. Here, we use the work function of the bulk of 5 eV for SiO_2[18] as a first approximation for W. For a 130 nm diameter NP, the energy balance predicts that charging a NP with a charge above 300 e (500 e) is not possible for O_2 (Ar) gas. When neglecting W, the electron abstraction limit is at a NP charge of about 550 e (700 e) for O_2 (Ar) gas. In practice, much higher NP charges are easily reached.

In the following, we probe the charging rate k_{total} of individual SiO_2 NPs in an ion trap at room temperature over a large range of positive charges by exposing the NPs to charge carriers generated by a cold cathode pressure gauge. We demonstrate that the NP charge can be manipulated in a controlled way by adjusting the pressure, the buffer gas type in the trap chamber and the trap potential. The gases investigated are Ar, N_2, O_2, and He. Exploring different amplitudes and waveforms of the ion trap potential using a high-precision programmable waveform generator reveals its influence on the charging and discharging dynamics. The mechanisms underlying NP charging and discharging are evaluated with respect to the type, origin, number and kinetic energy of the involved charge carriers. A simple model considers electron abstraction by gas cations and electron attachment. It is complemented by simulations of electron and ion motion in the trap region that provide evidence of the important role of the trap potential to reach significantly higher NP charges than expected from the IPs of the NP and gases.

Methods

Experimental

Suspensions of silica NPs (Nanocomposix) with a nominal diameter of 100 nm in water were used. The NPMS instrument and the measurement principle is briefly described here and in detail elsewhere.[3,6] NPs are introduced into the NPMS instrument by electrospray ionization (ESI). They are trapped in a split-ring electrode Paul-type ion trap optimized for large optical access. A cross section of the ion trap is shown in Fig. 3. The radiofrequency trapping potential is applied to the split-ring electrode and the end-cap electrodes (blue and red electrodes, respectively, in Fig. 3). For mass spectrometry, trapped NPs are irradiated by continuous-wave 532 nm radiation from a diode-pumped solid-state laser (Gem 532, Laser Quantum GmbH) with a power of 4 mW. The beam diameter in

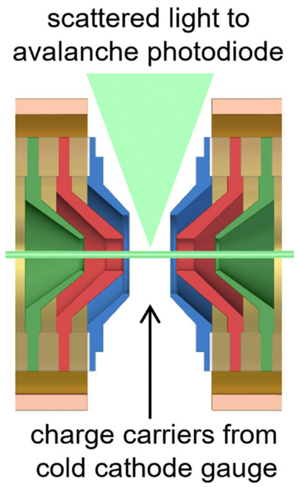

Fig. 3 Schematic cross section of the ion trap with the split-ring electrode (blue) and the end-cap electrodes (red). The excitation electrodes (green) are used for resonant excitation of the particle motion. The laser (horizontal light green line) is aligned along the cylindrical trap axis. The light scattered by the NP is measured by an avalanche photodiode. A cold cathode gauge generates charge carriers that can change the NP charge.

Open Access Article. Published on 18 February 2026. Downloaded on 5/10/2026 3:55:05 AM.
This article is licensed under a Creative Commons Attribution 3.0 Unported Licence.

the trap center is 1.08 mm. The light scattered by the NP is detected by an avalanche photodiode (Count 50 C, Laser Components) which is mounted perpendicular to the laser beam. A periodic voltage of 5 V is applied to the excitation trap electrodes (green electrodes in Fig. 3) and its frequency is scanned to determine the secular frequency of the NP by resonant excitation of its motion.[2] The secular frequency is proportional to the mass-to-charge ratio. Absolute charge and mass are deduced from secular frequency steps between different NP charges.

The gas flow into the trap was adjusted using a mass flow controller (EL-FLOW Prestige, Bronkhorst). During NP trapping, Ar gas was set to a pressure of 7×10^{-2} mbar with a needle valve while opening the mass flow controller. For experiments on charging dynamics, gas type and pressure were varied. The pressure during mass spectrometry intervals was constant at 3×10^{-3} mbar. The gas flow was converted to absolute pressure using a gas-type independent capacitance manometer (627F Baratron, MKS) that was attached to the ion trap by a Teflon tube. The capacitance manometer reading was corrected for thermal transpiration.[19] The lowest pressures could only be reached by closing the mass flow controller and pumping down to a desired pressure range. In this case, pressures were measured with a cold cathode gauge (WRG-S, Edwards Vacuum) that was calibrated to the absolute pressure at low gas flows and mounted such that it does not interact with the trapped NP.

The polarity of the NP charge was determined by observing the movement of the light scattered by the NPs on a sCMOS camera (Marana 4.2B-6, Andor) when the NP is attracted or repelled by a potential applied to two metal rods above the ion trap.

Sinusoidal trap potentials were generated by a function generator (33510B, Keysight) and a home-built amplifier. As an exception, experiments with alternating waveforms or amplitudes were carried out with an audio- and radiofrequency generator for output voltages of up to ±400 V and frequencies up to about 100 kHz (HV-AMP400FN-2D, CGC Instruments) that allows to define arbitrary waveforms and switch between them during trapping without interrupting the signal output. Besides a sine wave, a sinusoidal waveform interrupted by gaps of zero potential between the half cycles was used. The transitions between sine wave and gaps were rounded off to reduce high harmonics in the frequency spectrum that would be distorted by the amplifier. The trap frequency was kept at 25 kHz throughout the experiments with the stability parameter q_z typically staying below 0.3, such that no frequency adjustment was required for stable trapping.

Charge changes ΔQ of the NP were induced by turning on a wide range pressure gauge (WRG-S, Edwards Vacuum) which contains a cold cathode gauge (along with a Pirani element that does not influence the NP charge) for a designated time Δt (see Fig. 4). The distance between gauge and trap center was 20 cm for most experiments except those with varied waveform settings, where the distance was 40 cm. An aluminum foil with cutouts is installed between gauge and trap center, blocking the central line of sight to reduce the stream of photons and charge carriers coming from the gauge (see Fig. S2). Charging intervals (without laser irradiation) at varying pressures were alternated with secular frequency measurements (from which Q is derived) at constant pressure, since the latter were disturbed by light emitted from the plasma in the cold cathode gauge.

To sample different pressures at all Q, different pressure values were cycled through during relatively short durations with similar Q (see Fig. 4b). The waveform and amplitude were only modified during charging intervals and alternated between successive charging intervals of identical pressure to ensure comparable sampling. A Python program allows to define flexible experimental sequences, in particular to decouple charging and mass spectrometry intervals. It communicates *via* TCP/IP with a Labview program for device control and automated monitoring of the secular frequency.

To obtain information on the pressure dependence of the number of electrons present in the trap while the cold cathode gauge is turned on, the end-cap electrodes closest to the trap center (red in Fig. 3) were connected to a picoamperemeter (9103, RBD Instruments) with a bias potential of +90 V. During current measurements, the trap potentials were inactive.

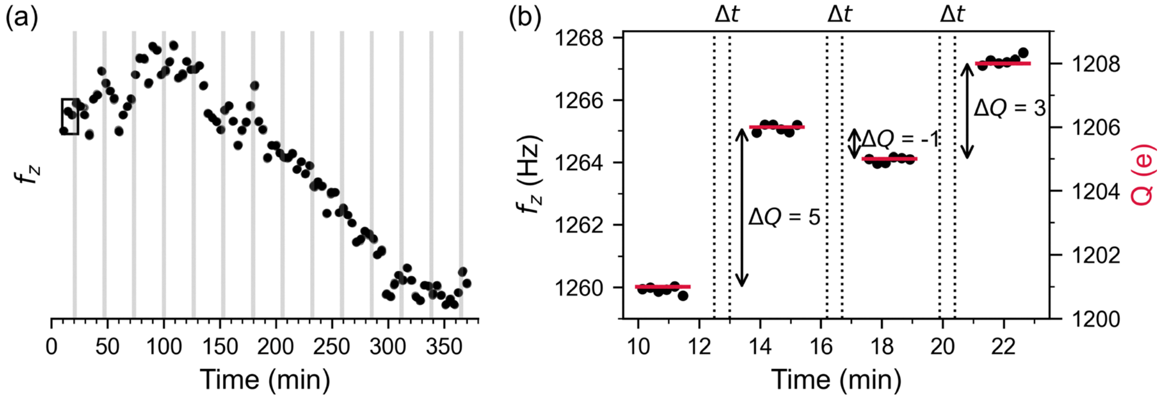

Fig. 4 NP Secular frequency f_z as a function of time. (a) Example of a measurement cycling through seven different pressure values during charging, one of which is shaded in gray. A zoom of the black box is shown in (b). (b) The NP charge Q (red bars) is derived from the NP secular frequency (black dots). The cold cathode gauge is active in time intervals Δt to induce charge changes ΔQ.

Open Access Article. Published on 18 February 2026. Downloaded on 5/10/2026 3:55:05 AM.
This article is licensed under a Creative Commons Attribution 3.0 Unported Licence.

Simulations

Simulations were performed with the SIMION 8.1 software.[20] Electron and cation trajectories were calculated based on a given trap geometry. As input parameters, the starting position, direction, electron kinetic energy, Ar cation kinetic energy as well as the initial phase of the oscillating trap potential were varied. Simulations were also carried out for different waveforms and amplitudes. A sphere with a diameter of 0.3 mm was used as criterion when ions or electrons reach the trap center. The presence of gas was neglected as the mean free path for an Ar atom (or cation) for the highest investigated pressure of 5×10^{-3} mbar is 2 cm, which corresponds to the trap radius, and the mean free path for electrons exceeds the longest calculated electron trajectories.

Data evaluation and visualization

The data were grouped by pressure and NP charge. For presentation, either a NP charge subset of the data was grouped by pressure and k_{total} was plotted against the pressure (as in Fig. 5a) or *vice versa* (as in Fig. 5b). For each group, the charging rate k_{total} was determined by dividing the total charge change $\Sigma\Delta Q$ by the cumulative time the gauge was active $\Sigma\Delta t$. Error bars for each group represent the standard error of the mean charging rate, calculated as the standard deviation of the individual charging rates $\frac{\Delta Q}{\Delta t}$ within each interval Δt divided by the square root of the sample size.

Results and discussion

Spontaneous charge changes of a trapped NP occur about once per day. In contrast, the NP charge changes as soon as the cold cathode gauge is active, which is consequently the only relevant source of charge carriers. Both positive and negative charge changes ΔQ of the positively charged NPs are measured within time intervals Δt under all applied experimental conditions. This shows that at least two charging mechanisms of opposite sign contribute to the observed ΔQ values.

The role of buffer gas type, pressure and NP charge

Fig. 5 illustrates the dependence of the charging rate k_{total} on (a) pressure p and (b) NP charge Q for a single NP with different buffer gases. It focuses on experimental conditions for which electron abstraction is expected to be efficient due to (a) low Q and (b) high pressure. The expectation that k_{total} increases with higher pressure (see Fig. 2(3)) is confirmed by the data shown in Fig. 5a, except at the respective highest Ar and N_2 gas pressures. The charging rate is highest for Ar and lowest for O_2. While k_{total} remains predominantly positive across the examined pressure ranges for Ar, N_2, and He, it is mostly negative for O_2. Fig. 5b shows k_{total} as a function of Q. With higher Q, k_{total} decreases for all gases, which is partly explained by the linearly decreasing cation–NP collision cross section in eqn (1), except for Ar and O_2 between 600 and 800 *e*. The available He data at low Q show similar low charging efficiency as for O_2. Ar only exhibits a higher k_{total} than N_2 around 800 *e*. An equilibrium between charging and discharging rate is reflected in the maximum charges $Q_{\max}$, at which k_{total} becomes zero—meaning further charging under the same conditions is no longer possible. For a 130 nm diameter NP, $Q_{\max}$ is around 1400 *e* for Ar and around 900 *e* for O_2 (see Table S1 for all NP diameters). These values represent soft limits, as k_{total} was averaged over a range of pressures (see figure caption). The Ar and O_2 data were obtained from three NPs of different sizes which may result in slight variations in surface potentials and thus $Q_{\max}$.

Fig. 6 shows complementary data to Fig. 5 for high Q and low pressures (inset) where electron abstraction is expected to be less and electron attachment to be more efficient. Indeed, at high Q (empty markers), k_{total} with O_2 is negative over the entire pressure range. As expected, a high Q facilitates discharging,

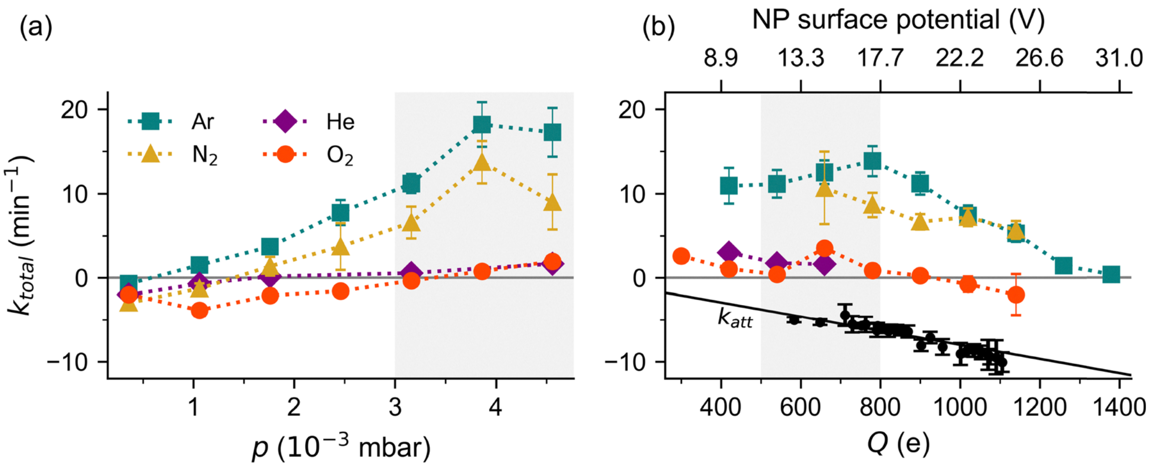

Fig. 5 Charging rates k_{total} with different buffer gases (Ar, N_2, He, O_2) plotted against (a) pressure p at low NP charge Q (500 to 800 *e*) and (b) charge Q at high p (3×10^{-3} mbar to 5×10^{-3} mbar). Gray shaded areas show the selected experimental range for the respective other figure. Dotted lines serve to guide the eye. The upper axis in plot (b) gives the surface potential of a 130 nm diameter NP. The electron attachment rate k_{att} is plotted against Q (black dots) and fitted (black line) for O_2 and N_2 data (for details see section on the electron abstraction probability below).

Open Access Article. Published on 18 February 2026. Downloaded on 5/10/2026 3:55:05 AM.
This article is licensed under a Creative Commons Attribution 3.0 Unported Licence.

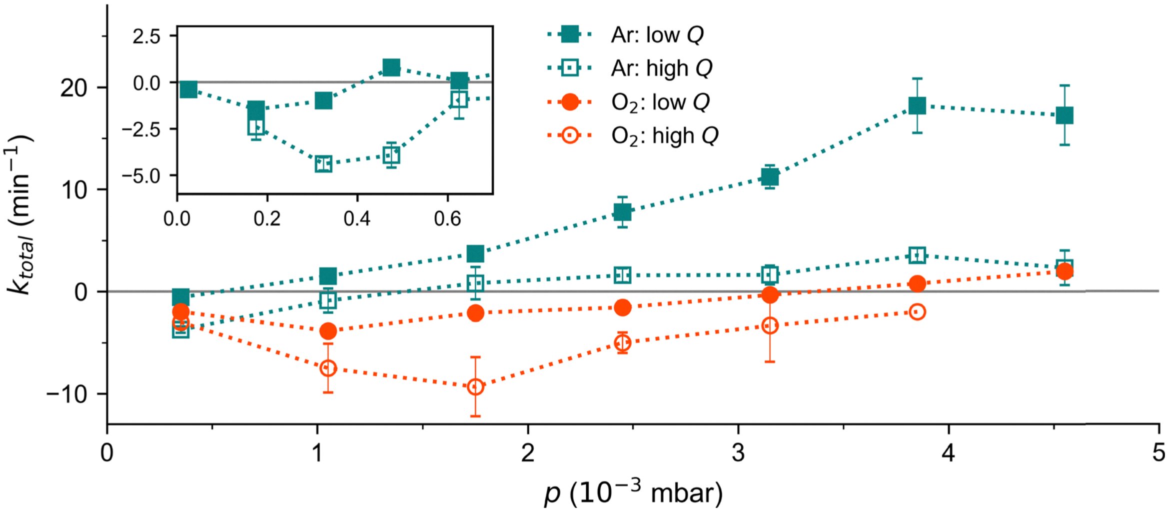

Fig. 6 Charging rate k_{total} plotted against the pressure p for Ar (green) and O_2 gas (orange) for low NP charge Q = 500 to 800 e (filled markers, as in Fig. 5a) and high Q = 1100 to 1300 e (empty markers). The inset shows a zoom of the low-pressure range for Ar gas. The error bars indicate statistical uncertainties. Dotted lines serve to guide the eye.

while a low Q fosters charging. An immediate practical implication of these results is that NPs can be efficiently charged with high Ar pressure and discharged with low O_2 pressure.

All gases exhibit an approximately linear pressure dependence of k_{total} (see Fig. S8), except for deviations at the lowest and highest pressures. The inset in Fig. 6 reveals that for Ar, k_{total} initially decreases up to 0.4×10^{-3} mbar before increasing again—similar to the behavior in Fig. 2(3a). In other words, discharging becomes more efficient with increasing pressure at first, but less efficient beyond a certain threshold. O_2 shows a comparable trend, though the transition to increasing k_{total} occurs only above 2.5×10^{-3} mbar. In comparison to Fig. 2(3a and b), these findings suggest that the electron number increases with rising pressure up to $\approx 0.5 \times 10^{-3}$ mbar for Ar and $\approx 3 \times 10^{-3}$ mbar for O_2 and is approximately constant above that. This is supported by measuring the electric current on the ion-trap electrode located closest to the ion-trap center (see Fig. S3): the number of electrons in the trap at first increases with rising pressure to a local maximum, then decreases (only for Ar and He) and is roughly constant above $\approx 10^{-3}$ mbar; for O_2, it is still slightly increasing up to $\approx 3 \times 10^{-3}$ mbar. At low pressure, the number of electrons reaching the ion trap increases with pressure, as collisions with gas species are negligible (see mean free path based calculation in Fig. S1a). At higher pressures, the balance between primary electron formation (expected to scale linearly with pressure), electron loss *via* collisions (likely to scale exponentially), and secondary electron production by electron impact ionization leads to a near-constant electron density in the trap.

The empirical results discussed so far support the expected charging mechanisms presented in the introduction: negative k_{total} values at low pressure and the electric current measurements indicate the presence of electrons in the trap and the dominance of electron attachment over electron impact ionization of the NP and electron abstraction by gas cations. The observed increase of positive k_{total} values with higher pressure indicates that charging is caused by the presence of gas cations. It also shows that the influence of gas cations possibly emitted by the gauge is of little importance: at low pressures, electron attachment is dominant, and at higher pressures, gas cations will be strongly suppressed by collisions before reaching the trap due to a shorter mean free path (see Fig. S1a). We conclude that the gas cations that drive electron abstraction are produced by electron impact ionization in the trap region. The finding that a high Q reduces charging and fosters discharging qualitatively agrees with the increasing IP of the NP for higher Q.

The role of the ion trap potential

It is, however, striking that the experimentally determined maximum charges $Q_{\max}$ in O_2 and Ar atmosphere of up to 900 e and 1400 e (see Fig. 5b) for a NP with $\approx$130 nm diameter (see Table S1 in the SI) are much higher than the limits for electron abstraction *via* thermal gas cations at $Q \approx 300$ e and 500 e, respectively, according to eqn (3). The energy balance thus cannot be interpreted as the IP of the gas cation providing the required energy to abstract an electron from the NP. In the diffusion charging mechanism, Brownian motion makes ions collide with initially neutral particles. For our case, electron abstraction from the NP surface by a colliding cation neutralizes the latter which can then freely leave the NP surface. If the IP of the neutral gas is higher than the work function at the NP surface, electron abstraction is thus possible as long as cations collide with the NP. This limits diffusion charging of a 130 nm NP to a charge of few elementary charges that cause a Coulomb repulsion that surpasses thermal kinetic energies at room temperature. It thus becomes clear that gas cations with high kinetic energies need to drive NP charging to high charges. The neutral gas is thermal such that high kinetic cation energies

Open Access Article. Published on 18 February 2026. Downloaded on 5/10/2026 3:55:05 AM.
This article is licensed under a Creative Commons Attribution 3.0 Unported Licence.

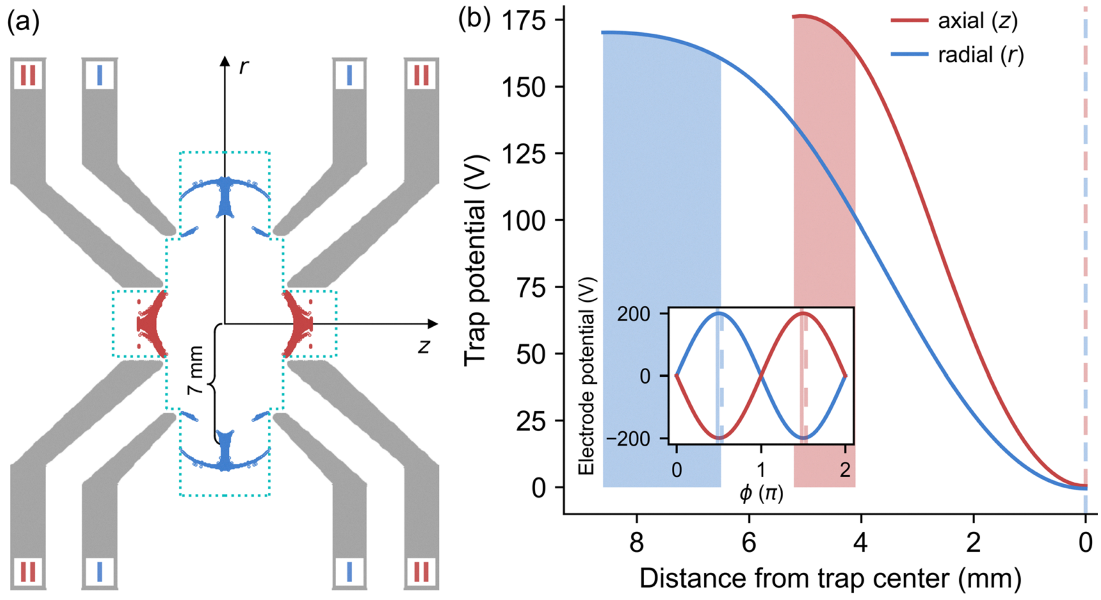

Fig. 7 (a) Starting positions of gas cations that reach the trap center with a kinetic energy above 160 eV. (b) The trap potential in radial (blue) and axial (red) direction at a phase of 0.5π and 1.5π. The inset shows the corresponding potential (200 V amplitude, sine waveform) applied to the split-ring electrode and the end-cap electrode (gray, marked with I and II, respectively, in panel (a)). The inset further shows the start (solid lines) and end (dashed lines) times of the cations for motion in axial and radial direction in light red and light blue, respectively. In panel (b), the corresponding start locations of the cations are depicted as light blue and red areas, the end location in the trap center as a dashed line. The starting positions for all simulated cations were equally distributed over the area enclosed by turquoise dotted lines.

can only be reached by acceleration of the nascent ions in the trap potential which is discussed in the following.

The trap frequency of 25 kHz used to trap NPs is too low to trap thermal gas cations and electrons with much lower mass-to-charge ratios, but they are still accelerated in the trap potential. The motion of cations in the trap was calculated for different starting positions and phases of the trap potential, and with initially zero kinetic energy since thermal energy is mostly negligible. The starting positions were equally distributed over the area enclosed by turquoise dotted lines in Fig. 7a. The simulations show that only ions that are formed in specific regions and at an adequate phase of the trap potential reach the trap center. The following discussion focuses on the maximum possible acceleration that corresponds to the limit of electron abstraction from the NP. The highest acceleration is achieved from starting positions close to the trap electrodes at the phases of maximum potential. The two regions from which ions starting at opposing phases reach the ion trap center with kinetic energies of 160 eV and higher are depicted by colored areas in radial (blue) and axial (red) direction close to the split-ring electrode and the end-cap electrode, respectively (the colors correspond to the electrodes in Fig. 3 that are additionally denoted by I and II in Fig. 7a). The waveforms of the trap electrode potentials (with a maximum of 200 V) are plotted against the phase for radial and axial direction, respectively, in the inset in Fig. 7b. The phases of start and end time of the fastest cations are depicted by light solid and dashed lines, respectively. The electrode potential is nearly the same at the start and end time of the cation motion towards the trap center. Therefore, the ion acceleration is essentially captured by static potentials that are plotted along the radial and axial symmetry axes in Fig. 7b. Due to the R^{-1} dependence, gas cations only significantly experience the Coulomb barrier when their distance from the NP is less than about 1 μm. Consequently, gas cations are accelerated until they reach the trap center with their final speed, which is then available to overcome the Coulomb barrier.

The acquired kinetic energy depends on the initial distance from the ion trap and can reach values of above 170 eV which allows gas cations to overcome the Coulomb potential of a 130 nm NP up to a charge of almost 8000 e (see Fig. S4). Taking into account the trap potential as a driver of NP charging, both the (phase dependent) kinetic energy E_{kin} of the accelerated gas cations and the IP of the gas species contribute to the energy balance of the two-step electron abstraction process:

$$\Delta E_{\mathrm{abst}} = E_{\mathrm{kin}} - \frac{Qe}{4\pi\epsilon_0 R} + \mathrm{IP}_{\mathrm{gas}} - W. \tag{4}$$

Gas cations can only be accelerated to high kinetic energies if they are generated by electron impact ionization at the previously described specific locations and phases. Therefore, we now consider for which potential phases electrons can access which trap regions. In the first half cycle (0 to π) of the potential along the radial axis, the ideal location for maximum acceleration of cations is close to the saddle point of the positive potential at the outer edges of the blue regions in Fig. 7a. At the same time, electrons approaching from the gauge are attracted to this region. During most phases in the first half cycle, they are sufficiently accelerated by the trap potential to induce electron impact ionization, regardless of their initial

Open Access Article. Published on 18 February 2026. Downloaded on 5/10/2026 3:55:05 AM.
This article is licensed under a Creative Commons Attribution 3.0 Unported Licence.

speed. The axial red region at opposite phase (see Fig. 7a) is less important for cation generation and acceleration, as electrons are blocked by a barrier from entering and will not be easily steered to these geometrically hidden regions.

Having established the importance of cations that originate from the blue region in Fig. 7a at about 7 mm distance from the trap center, we note that at the highest investigated pressure of 5×10^{-3} mbar, only 60% of the ions reach the trap center due to their decreased mean free path (see Fig. S1b). The linear trend in Fig. 5a will therefore be suppressed at pressures beyond the range investigated here.

The finding that the trap potential accelerates cations raises the expectation that a higher trap amplitude leads to a higher $Q_{\max}$ due to increased kinetic energies of the gas cations. Conversely, an interrupted trap potential should lead to a lower k_{total} because for a fraction of the period neither electrons nor cations (that are produced by the fast electrons) are accelerated while slow electrons can freely pass to the trap center. Simulations of the electron motion in the trap (see Fig. S5) show that the sine waveform works as a filter that hinders slow electrons from reaching the trap center. Using a waveform with a gap significantly increases the fraction of slow electrons reaching the center region (see Fig. S5 and S6), which is favorable for electron attachment. Indeed, experiments confirm that higher trap potentials lead to a higher k_{total} (Fig. 8) and a higher $Q_{\max}$ (Fig. 9) while an interrupted waveform fosters discharging (Fig. 8). We measured k_{total} with Ar for (A) a higher amplitude of 238 V of the trap electrode potential compared to (B) the standard sine waveform with 200 V amplitude and to (C) a sine with gaps of zero potential and an increased amplitude of 238 V, such that the secular frequency of the NP remains unchanged relative to (B). The results show that k_{total} rises with higher trap potential for the same waveform (settings A and B). Comparing the different waveforms for the same amplitude of 238 V (settings A and C) shows that discharging in the lower pressure range is more efficient for a sine with gaps, even despite the strong opposite effect of the higher amplitude. A quantitatively similar effect is seen at 200 V amplitude and low NP charge, where charging is generally more favorable (see Fig. S7). Synchronizing a pulsed electron source with the potential gaps could significantly enhance discharging rates and open the door to increase the negative charge of anionic NPs which could not be achieved with the present setup.

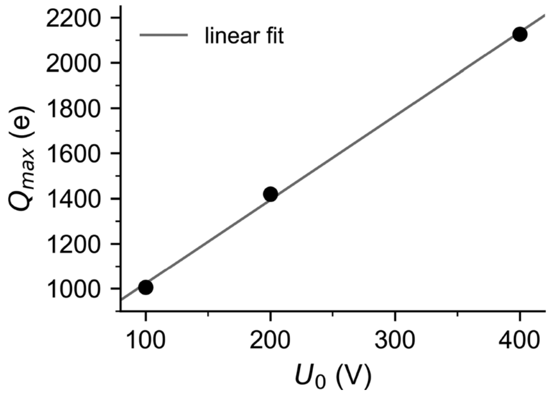

Fig. 9 Maximum NP charge $Q_{\max}$ as a function of trap potential amplitude U_0 at which the NP was charged at an Ar pressure of 3.5×10^{-3} mbar. The linear fit yields $Q_{\max} = (3.71 \pm 0.15)\ e\ \text{V}^{-1} \times U_0 + (652 \pm 40)\ e$.

The results confirm the strong influence of the amplitude on the maximum charge that we concluded from the discrepancy between the observed maximum charge (Fig. 5b), the Coulomb barrier of the NP and the simulations described above. A linear fit of the maximum charge *versus* trap electrode potential amplitude at constant pressure in Fig. 9 shows that an increase of 1 V in amplitude enables the NP to gain approximately 4 additional elementary charges. The extrapolated experimental $Q_{\max}$ of about 650 e at vanishing potential lies within the Q limits for electron abstraction of 500–700 e in the energy balance in eqn (3) and suggests a work function below that of the bulk. The possibility to discharge NPs using a sine with

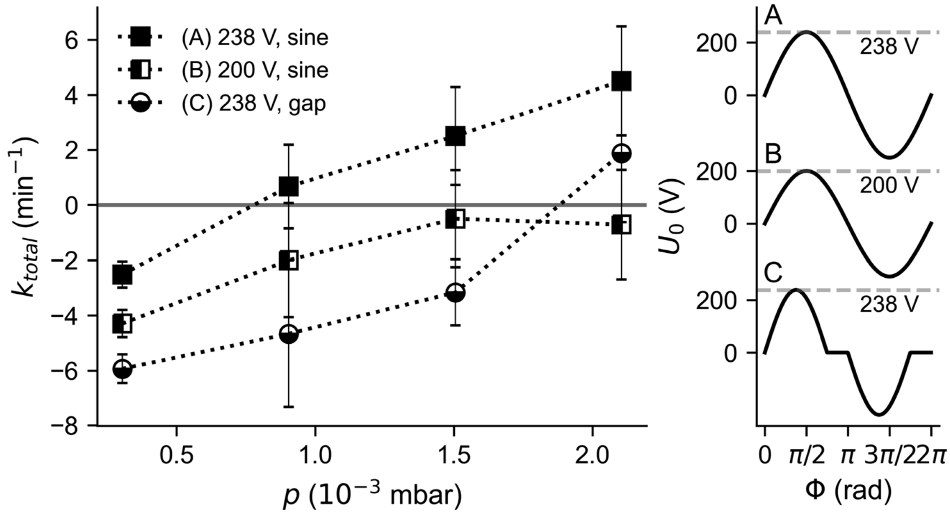

Fig. 8 Charging rate k_{total} for Ar gas as a function of the pressure p for different trap potential amplitude U_0 or waveform (A)–(C) and high NP charges Q from 1150 to 1450 e. Different amplitudes and waveforms are displayed on the right as a function of the phase Φ.

Open Access Article. Published on 18 February 2026. Downloaded on 5/10/2026 3:55:05 AM.
This article is licensed under a Creative Commons Attribution 3.0 Unported Licence.

gaps as a trap potential waveform (see Fig. 8) is beneficial in cases where inert experimental conditions are required and therefore O_2 should be avoided as a buffer gas.

In the present study, the trap frequency was kept constant. In reaction kinetics experiments, large changes in the NP mass-to-charge ratio may require adjustments of the trap frequency to maintain stable trapping.[21] Such adjustments are not expected to significantly affect charging rates, as the trap frequency remains low compared to electron and ion motion, and thus allows the above static description.

While we chose the cold cathode gauge as an easily accessible electron source, the fact that the presence of the ion trap intrinsically leads to broad electron kinetic energy distributions shows that an electron source with a well defined distribution would probably provide little additional insight.

Electron abstraction probability and charging limits

In this section, the NP charging rate k_{total} is separated into the electron abstraction rate k_{abst} and the electron attachment rate k_{att} by fitting k_{total} as a function of pressure p. Factorizing k_{abst} into a gas-type independent constant and the gas-type dependent electron abstraction probability allows a comparison of the fit results for different gases with the respective gas IPs and electron impact ionization cross sections. Subsequently, the dependence of k_{abst} and k_{att} on Q is explored. Extrapolating k_{att} to large Q yields charging limits, which are finally compared to the experimental $Q_{\max}$ values and the simulation results from the previous section.

The experimental data recorded with standard trap potentials were fitted as a function of pressure p using the linear equation $k_{\text{total}} = mp - k_{\text{att}}$ for each gas and for the same Q range, respectively. Table 1 lists the fit results for the data in Fig. 5a (fits for all analyzed Q ranges are summarized in Fig. S9). The fits include only data above 10^{-3} mbar, where the electron density was found to be approximately constant. Thus, the intercept represents the pressure-independent electron attachment rate k_{att} in the pressure range above 10^{-3} mbar, and the slope $m = \frac{k_{\text{abst}}}{p}$ reflects the electron abstraction rate k_{abst} at 10^{-3} mbar.

Table 1 Linear fit parameters for k_{total}, slope m and intercept $- k_{\text{att}}$, as a function of p for Q = 500 to 800 e (see Fig. S8), as well as total electron impact ionization cross sections σ_{EI} averaged over electron kinetic energies from 30 eV to 200 eV with recommended values from ref. 22–25, ionization potentials IP_{gas} from ref. 26–31, and the ratio $m/(\sigma_{\text{EI}}k_{\text{att}})$. See text for details

Gas	$m = k_{\text{abst}}/p$ ($\mu\text{bar}^{-1}\ \text{min}^{-1}$)	k_{att} (min^{-1})	σ_{EI} (Å^2)	IP_{gas} (eV)	$m/(\sigma_{\text{EI}}k_{\text{att}})$ ($\mu\text{bar}^{-1}\ \text{Å}^{-2}$)
Ar	4.6 ± 0.4	3.4 ± 0.5	2.78	15.8	0.49 ± 0.08
N_2	4.0 ± 0.6	5.5 ± 1.0	2.26[a]	15.6 (N_2), 14.5 (N)	0.32 ± 0.08
O_2	1.59 ± 0.10	5.3 ± 0.3	2.20[a]	12.0 (O_2), 13.6 (O)	0.137 ± 0.012
He	0.60 ± 0.07	1.3 ± 0.2	0.32	24.6	1.44 ± 0.33

[a] The dominant ions are N_2^+ (O_2^+) and N^+ (O^+) with σ_{EI} values of 1.70 Å (1.42 Å) and 0.55 Å (0.77 Å).

To compare the fit results across gas types, we factorize k_{abst} into the cation–NP collision rate and the probability P_{abst} that a collision leads to electron abstraction:

$$k_{\text{abst}} = C\,p\,\sigma_{\text{EI}}\,k_{\text{att}}\,P_{\text{abst}} \tag{5}$$

The gas-independent constant C includes the cation–NP collision cross section in eqn (1), that depends on the kinetic energy of the gas cations and the charge-dependent surface potential of the NP. The cation density in the trap depends on the neutral gas pressure p, the electron impact ionization cross section σ_{EI}, and the electron density in the trap that is proportional to k_{att}, assuming that the electron kinetic energy distribution remains constant across gas types. Thus, the ratio $\frac{m}{\sigma_{\text{EI}}k_{\text{att}}} = CP_{\text{abst}}$ isolates the gas-type dependence of P_{abst}.

The results in Table 1 show that P_{abst} is largest for He and smallest for O_2, in line with the IPs of the neutral species. The exceptionally high IP of He makes electron abstraction favorable, but its low σ_{EI} leads to low electron and ion densities and, consequently, low overall charging rates at equal pressures. For O_2 and N_2, k_{att} and σ_{EI} are similar, implying that the favored discharging observed with O_2 arises solely from a lower P_{abst}. An additional discharging mechanism *via* electron transfer from O^- or O_2^- to the NP is unlikely, as the formation cross sections for O_2^+ exceed those for O^- by two orders of magnitude, and the formation of O_2^- by three-body collisions is negligible.[32]

With Ar, k_{att} is lower than with N_2 and O_2. Therefore, the enhanced charging observed with Ar not only results from an increased k_{abst} but also from a reduced k_{att}, the origin of which remains unclear. That k_{abst} (= mp) is still largest for Ar, despite its proportionality to k_{att} in eqn (5), is due to its 53% higher P_{abst} compared to that for N_2, even though the corresponding IPs for the two gases are almost identical. Another explanation could be a Penning ionization contribution to charging with Ar for $Q < 1000\ e$, where k_{abst} for Ar exceeds that for N_2 (see Fig. 5b). However, electrons released *via* this mechanism must escape the increasing surface potential of the NP, making it energetically inaccessible above 300–700 e (for a NP work function of 5–0 eV, a 130 nm diameter NP, and excitation energies from 11.5 to 15.5 eV).

As Q increases, the product CP_{abst} generally decreases for all gases (see Fig. S10). A higher (repulsive) Q linearly reduces the NP–cation collision cross section in eqn (1), and thereby C. It is conceivable that Q also alters P_{abst} by affecting the kinetic energy of the ion impact or the NP's work function.

To estimate the maximum Q for which electron abstraction is possible, we analyze the dependence of k_{att} on Q (see Table 1 and Fig. S9 for different Q ranges). The resulting O_2 and N_2 data are presented in Fig. 5b (black dots) with a linear fit (black line) according to the linear increase of the electron–NP collision cross section with NP charge in eqn (2). The negative slope reflects that k_{att} increases with the larger collision cross section.

We can now explore how the experimentally observed maximum Q (see Fig. 5b) relates to the electron abstraction limits (see eqn (4)) and assess their dependence on the trap potential (see Fig. 9). Electron abstraction is limited by the maximum Q

Open Access Article. Published on 18 February 2026. Downloaded on 5/10/2026 3:55:05 AM. This article is licensed under a Creative Commons Attribution 3.0 Unported Licence.

that allows cation–NP collisions, $Q^{\text{abst}}_{\max} = 4\pi\epsilon_0 R U_0 \approx 45\ e(U_0/\text{V})$, assuming a maximum ion kinetic energy eU_0 in eqn (4) and a 130 nm diameter NP. In contrast, the observed maximum charge with Ar buffer gas in Fig. 9 scales with $Q^{\text{total}}_{\max} \sim 3.7\ e(U_0/\text{V})$. We attempt a simultaneous linear fit of k_{total} and k_{att} that reconciles the different scaling with the trap potential U_0 in Section S8. The approach is not exact and fails with Ar and He data, but a good and decent match with N_2 and O_2 data in Fig. S11 shows that the different dependencies on the trap potential can in principle be explained by the NP charge dependence of k_{att}. The resulting Q limits for electron abstraction lie between 10 000 e and 20 000 e, and therefore exceed the energy limit for cation–NP collision by a factor of up to three (see Fig. S4), possibly because the model neglects any charge dependence of the electron attachment and electron abstraction probabilities upon collision of an electron or a cation with the NP, and likely due to the rather poor applicability of data extrapolation.

In the course of this article, we have discussed several empirical and theoretical charging limits. In diffusion charging, gas cations can overcome the Coulomb barrier of a NP only with a few charges. The energy balance for thermal cations in eqn (3) predicts an electron abstraction limit at $\approx$300 e (500 e) for a 130 nm NP in O_2 (Ar). Empirical data (see Fig. 5b) shows that electron abstraction dominates up to $\approx$900 e (1400 e) for O_2 (Ar), which reveals the important role of cation acceleration by the trap potentials and is a lower bound for the electron abstraction limit. Linear extrapolation of k_{att} to higher Q in Section S8 indicates much higher electron abstraction limits. This is consistent with simulation results indicating that gas cations can overcome the Coulomb barrier up to $\approx$8000 e for a 130 nm diameter NP at 200 V trap amplitude (see Fig. S4). This value lies well beyond the Rayleigh limit of $\approx$2500 e for liquid droplets and corresponds to surface potentials of $\approx$180 V. Much higher charge states have been reached for 500 nm diameter SiO_2 NPs with X-ray irradiation near 538 eV photon energy inducing resonant Auger processes.[8] In the cited study, a steady discharge due to residual gas ($\sim 10^{-8}$ mbar) or ion desorption was reported above 40 000 e ($\approx$230 V potential) and charges $>$60 000 e ($\approx$350 V potential). We typically use much higher pressures ($\sim 10^{-3}$ mbar) for the resonant excitation scheme to perform mass spectrometry and for buffer gas cooling in cryogenic experiments. We conclude that the charging will in this case be limited by a steady discharge due to buffer gas before reaching the linear extrapolation limit.

The role of the NP's initial charge, size and material

In case of different types of charge carriers from the initial ESI charging and later electron abstraction, the initial charge, possibly in form of Na^+ ions, could influence the charging rates. The available data do not provide information on this question. Instead, we estimate the charge per silica molecule on the surface: with 600 e as an empirical upper bound of the as-trapped NP charge, 130 nm NP diameter, Wigner Seitz radius $\sqrt[3]{3/4\pi n}$ with number density n (derived from the silica bulk density of 2.65 g cm^{-3}), and hexagonal packing, one obtains less than 1 initial charge carrier per 600 surface SiO_2 molecules. This coverage seems too small to have a significant effect on the charging rates that are caused by interactions with electrons (mediated by Coulomb attraction and energy dissipation by surface collisions) and ions (mediated by electron transfer from the NP surface to a colliding ion).

For the practical application of the reported results, it is also important to consider the role of the NP size, given by radius R. As the NP surface potential, ionization potential and electron affinity depend on the ratio Q/R, see eqn (4) and Section S10 of the SI, the discussed trends as a function of NP charge Q similarly hold for changes of the inverse NP radius R^{-1}. In addition to the dependence on Q/R, the collision cross sections of cations and electrons with a NP in eqn (1) and (2) scale with the geometric cross section πR^2. Disregarding possible effects of the surface charge on electron attachment and electron abstraction probabilities upon collision of an electron or a cation with the NP, we can summarize that all charging rates are expected to increase quadratically with NP size and that the ratio of the electron abstraction and attachment rates decreases monotonously with Q/R,

$$\frac{k_{\text{abstr}}}{k_{\text{att}}} \propto \frac{\sigma^{\text{cation-NP}}_{\text{coll}}}{\sigma^{\text{electron-NP}}_{\text{coll}}} = \frac{1-\left(\dfrac{Q}{R}\right)e\Big/\left(4\pi\epsilon_0 E^{\text{cation}}_{\text{kin}}\right)}{1+\left(\dfrac{Q}{R}\right)e\Big/\left(4\pi\epsilon_0 E^{\text{electron}}_{\text{kin}}\right)}. \tag{6}$$

The pressure and charge dependencies reported in this work should therefore be largely applicable to different NP sizes when considering scaled rates k/R^2 and scaled charges Q/R. In case of negatively charged NPs, the sign of Q changes such that eqn (6) monotonously increases with $|Q/R|$. Consequently, electron attachment is favored for small $|Q/R|$, that is large NP radius R: the lower surface potential for large R reduces both the enhancement of the collision cross section for cations due to Coulomb attraction and the suppression of the collision cross section for electrons due to Coulomb repulsion. Thus, larger NPs are beneficial for future attempts to negatively charge anionic NPs.

Charging rates were also measured for $\approx$50 nm diameter Au NPs at low Q (300–750 e), which allows a comparison with a different NP material. However, the previous discussion on the size dependence advises to compare scaled rates k/R^2. As the NP surface potential scales with Q/R (see eqn (3) and (6)), these charging rates are additionally compared to those of $\approx$100 nm SiO_2 NPs at approximately twice the NP charge, $2Q$. The effect of the work function is less clear, as its bulk value is similar to that of SiO_2 and it significantly decreases for smaller NPs.[33,34] Empirical results show that also for 50 nm Au NPs, k_{total} decreases with higher Q and higher pressure (Fig. S12a), which is in line with the SiO_2 data. Across the measured Q range, k_{total}/R^2 is notably higher for Au NPs compared to SiO_2 NPs, which is even more pronounced in comparison to SiO_2 data with charge $2Q$ (Fig. S12b and c). The present data only allows to speculate

Open Access Article. Published on 18 February 2026. Downloaded on 5/10/2026 3:55:05 AM.
This article is licensed under a Creative Commons Attribution 3.0 Unported Licence.

that a lower work function of Au at 50 nm diameter or the charge delocalization in the metallic NP may contribute to higher electron abstraction probabilities. Extended data with different NP sizes for the same material and different NP materials for the same NP size will be needed to clarify the situation and to establish a quantitative correspondence between charging rates and NP material.

Conclusions

Measuring single particle charging rates of cationic 100 nm diameter SiO_2 NPs in an ion trap under different experimental conditions revealed the importance of the trap potential to charge NPs. The results demonstrate controlled discharging of positively charged NPs with a cold cathode gauge. Using O_2 gas, discharging was achieved even at pressures up to $\sim 10^{-3}$ mbar, which is attributed to a lower electron abstraction probability due to the lower IP of O_2 compared to other gases. Discharging was also successful using Ar gas with a tailored waveform for the trap potentials instead of O_2, allowing inert measurement conditions. Among the buffer gases studied (Ar, N_2, O_2, and He), Ar proved to be the most efficient for charging NPs, particularly at high pressure and high trap amplitude. In contrast, even though He^+ exhibits a higher electron abstraction probability (from a NP) than Ar^+ does, He's lower electron impact ionization cross section makes He gas inefficient for charging. Knowledge on the dependence of the different charging mechanisms on experimental conditions allows to control the charging/discharging rate, a prerequisite for performing efficient experiments to investigate the charge-state dependent properties of a single NP. Charging of 50 nm diameter Au NPs with Ar gas depends on pressure and charge in a similar way.

Our results corroborate that electron abstraction by gas cations and direct electron attachment are the dominant charging mechanisms. However, neither diffusion charging by thermal gas cations nor the energy balance for electron abstraction by thermal gas cations can explain the obtained high NP charges. We demonstrate that the ion trap radio frequency potential is the main driver of electron abstraction. The trap potential accelerates gas cations, enabling them to overcome the NP's repulsive surface potential. The generation of gas cations in the trap by electron impact ionization is also steered by the trap potential, as it accelerates incoming electrons. Efficient discharging *via* electron attachment therefore can be enhanced using a waveform generator capable of generating customized waveforms including zero-potential gaps, thereby preventing acceleration of electrons and ions and admitting slow electrons to the trap center.

Author contributions

Sophia C. Leippe: investigation (equal), formal analysis (lead), visualization, writing – original draft (lead), writing – review & editing. Kleopatra Papagrigoriou: investigation (equal), formal analysis (supporting). Carl Behrendt: investigation (waveform with gap). Björn Bastian: conceptualization, investigation (initial experiments, picoamperemeter measurements and simulations), software, formal analysis (supporting), validation, writing – original draft (supporting), writing – review & editing.

Conflicts of interest

There are no conflicts to declare.

Data availability

Datasets and analysis routines are available from the corresponding author upon reasonable request.

Supplementary information (SI) with additional tables, figures, and derivations. See DOI: https://doi.org/10.1039/d5cp04304b.

Acknowledgements

This work was funded by Deutsche Forschungsgemeinschaft (DFG) under grant number 461913655 (Einzelnanopartikelcharakterisierung in der Gasphase). S. L. acknowledges the Hans-Böckler-Stiftung and the DFG Project ID 443871192 – GRK 2721: "Hydrogen Isotopes, ^{1,2,3}H" for financial support. B. B. and K. P. acknowledge support from the Pre-Doc Award program at Leipzig University. K. P. acknowledges a Kekulé scholarship by the Fonds der Chemischen Industrie. We thank Ivo Cermak for support with the programmable waveform generator, Jiaye Jin for helpful discussions and Knut Asmis for ongoing support.

References

1 S. Schlemmer, J. Illemann, S. Wellert and D. Gerlich, Nondestructive High-Resolution and Absolute Mass Determination of Single Charged Particles in a Three-Dimensional Quadrupole Trap, *J. Appl. Phys.*, 2001, **90**, 5410.
2 C. R. Howder, D. M. Bell and S. L. Anderson, Optically Detected, Single Nanoparticle Mass Spectrometer with Pre-Filtered Electrospray Nanoparticle Source, *Rev. Sci. Instrum.*, 2014, **85**, 14104.
3 T. K. Esser, B. Hoffmann, S. L. Anderson and K. R. Asmis, A Cryogenic Single Nanoparticle Action Spectrometer, *Rev. Sci. Instrum.*, 2019, **90**, 125110.
4 B. Hoffmann, T. K. Esser, B. Abel and K. R. Asmis, Electronic Action Spectroscopy on Single Nanoparticles in the Gas Phase, *J. Phys. Chem. Lett.*, 2020, **11**, 6051.
5 B. Hoffmann, S. Leippe and K. R. Asmis, Probing the Electronic Absorption Spectrum of Single Gold Nanoparticles in the Gas Phase, *Mol. Phys.*, 2023, e2210454.
6 S. C. Leippe, F. Johst, B. Hoffmann, S. Krohn, K. Papagrigoriou, K. R. Asmis, A. Mews and B. Bastian, Probing the Temperature of Single Quantum Dots Confined in a Nanoparticle Ion Trap by Fluorescence Thermometry, *J. Phys. Chem. C*, 2024, **128**, 21472.

Open Access Article. Published on 18 February 2026. Downloaded on 5/10/2026 3:55:05 AM.
This article is licensed under a Creative Commons Attribution 3.0 Unported Licence.

7 J. Pavlů, I. Richterová, Z. Nemecek, J. Safránková and I. Cermák, Interaction Between Single Dust Grains and Ions or Electrons: Laboratory Measurements and Their Consequences for the Dust, *Faraday Discuss.*, 2008, **137**, 139–155.

8 M. Grimm, B. Langer, S. Schlemmer, T. Lischke, U. Becker, W. Widdra, D. Gerlich, R. Flesch and E. Rühl, Charging Mechanisms of Trapped Element-Selectively Excited Nanoparticles Exposed to Soft X Rays, *Phys. Rev. Lett.*, 2006, **96**, 66801.

9 M. A. Philip, F. Gelbard and S. Arnold, An Absolute Method for Aerosol Particle Mass and Charge Measurement, *J. Colloid Interface Sci.*, 1983, **91**, 507.

10 G. Hars and Z. Tass, Application of Quadrupole Ion Trap for the Accurate Mass Determination of Submicron Size Charged Particles, *J. Appl. Phys.*, 1995, **77**, 4245.

11 P. Kulkarni, N. Namiki, Y. Otani and P. Biswas, Charging of Particles in Unipolar Coronas Irradiated by In Situ Soft X-Rays: Enhancement of Capture Efficiency of Ultrafine Particles, *J. Aerosol Sci.*, 2002, **33**, 1279.

12 Y. Harada, S. Masuda and H. Ozaki, Electron Spectroscopy Using Metastable Atoms as Probes for Solid Surfaces, *Chem. Rev.*, 1997, **97**, 1897.

13 L. Schweikhard, P. Beiersdorfer, W. Bell, G. Dietrich, S. Krückeberg, K. Lützenkirchen, B. Obst and J. Ziegler, Production and Investigation of Multiply Charged Metal Clusters in a Penning Trap, *Hyperfine Interact.*, 1996, **99**, 97.

14 S. Schlemmer, S. Wellert, F. Windisch, M. Grimm, S. Barth and D. Gerlich, Interaction of Electrons and Molecules With a Single Trapped Nanoparticle, *Appl. Phys. A: Mater. Sci. Process.*, 2004, **78**, 629.

15 N. A. Fuchs, On the Stationary Charge Distribution on Aerosol Particles in a Bipolar Ionic Atmosphere, *Geofis. Pura Appl.*, 1963, **56**, 185.

16 K. Hansen. *Statistical Physics of Nanoparticles in the Gas Phase 73*, Springer Netherlands, Dordrecht, 2013.

17 I. Musa and J. Ghabboun, Work Function, Electrostatic Force Microscopy, Tunable Photoluminescence of Gold Nanoparticles, and Plasmonic Interaction of Gold Nanoparticles/Rhodamine 6G Nanocomposite, *Plasmonics*, 2025, **20**, 2531.

18 Y. D. Kim, T. Wei, S. Wendt and D. W. Goodman, Ag Adsorption on Various Silica Thin Films, *Langmuir*, 2003, **19**, 7929.

19 I. Yasumoto, Thermal Transpiration Effects for Gases at Pressures Above 0.1 Torr, *J. Phys. Chem.*, 1980, **84**, 589.

20 *SIMION Ion Optics Simulation Software Version 8.1*, Scientific Instrument Services, Inc., 2013.

21 A. M. Friese, A. R. Burrows and S. L. Anderson, High and Ultra-high Temperature Reaction Kinetics by Single Nanoparticle Mass Spectrometry, *Int. J. Mass Spectrom.*, 2025, **512**, 117435.

22 H. C. Straub, P. Renault, B. G. Lindsay, K. A. Smith and R. F. Stebbings, Absolute Partial and Total Cross Sections for Electron-Impact Ionization of Argon From Threshold to 1000 eV, *Phys. Rev. A: At., Mol., Opt. Phys.*, 1995, **52**, 1115.

23 Y. Itikawa, Cross Sections for Electron Collisions with Nitrogen Molecules, *J. Phys. Chem. Ref. Data*, 2006, **35**, 31.

24 Y. Itikawa, Cross Sections for Electron Collisions with Oxygen Molecules, *J. Phys. Chem. Ref. Data*, 2009, **38**, 1.

25 R. G. Montague, M. F. A. Harrison and A. C. H. Smith, A Measurement of the Cross Section for Ionisation of Helium by Electron Impact Using a Fast Crossed Beam Technique, *J. Phys. B: At. Mol. Phys.*, 1984, **17**, 3295.

26 Argon, in *NIST Chemistry WebBook, SRD 69*, ed. P. J. Linstrom and W. G. Mallard, National Institute of Standards and Technology, 2001.

27 S. G. Lias, Nitrogen, in *NIST Chemistry WebBook, SRD 69*, ed. P. J. Linstrom and W. G. Mallard, National Institute of Standards and Technology, 2001.

28 S. G. Lias, Nitrogen atom, in *NIST Chemistry WebBook, SRD 69*, ed. P. J. Linstrom and W. G. Mallard, National Institute of Standards and Technology, 2001.

29 S. G. Lias, Oxygen, in *NIST Chemistry WebBook, SRD 69*, ed. P. J. Linstrom and W. G. Mallard, National Institute of Standards and Technology, 2001.

30 S. G. Lias, Oxygen, atomic, in *NIST Chemistry WebBook, SRD 69*, ed. P. J. Linstrom and W. G. Mallard, National Institute of Standards and Technology, 2001.

31 S. G. Lias, Helium, in *NIST Chemistry WebBook, SRD 69*, ed. P. J. Linstrom and W. G. Mallard, National Institute of Standards and Technology, 2001.

32 Y. Itikawa, A. Ichimura, K. Onda, K. Sakimoto, K. Takayanagi, Y. Hatano, M. Hayashi, H. Nishimura and S. Tsurubuchi, Cross Sections for Collisions of Electrons and Photons with Oxygen Molecules, *J. Phys. Chem. Ref. Data*, 1989, **18**, 23.

33 W. Sachtler, G. J. H. Dorgelo and A. A. Holscher, The Work Function of Gold, *Surf. Sci.*, 1966, **5**, 221.

34 Y. Zhang, O. Pluchery, L. Caillard, A.-F. Lamic-Humblot, S. Casale, Y. J. Chabal and M. Salmeron, Sensing the Charge State of Single Gold Nanoparticles via Work Function Measurements, *Nano Lett.*, 2015, **15**, 51.